Journal of The Korean Astronomical Society
41: 163 ∼ 172, 2008 December

EXPANSION VELOCITY INVESTIGATION OF THE ELLIPTICAL PLANETARY NEBULA NGC 6803

Younsu Choi, Seong-Jae Lee, and Siek Hyung
School of Science Education (Astronomy), Chungbuk National University, Chungbuk 361-763, Korea
E-mail: hyung@chungbuk.ac.kr
(Received: October 16, 2008; Accepted: December 8, 2008)

ABSTRACT

Abstract: Using the spectral data in the 3700 to 10050$\AA$ wavelength range secured with the Hamilton Echelle Spectrograph (HES) at the Lick observatory, we have investigated the expansion velocities and the physical conditions of the elliptical planetary nebula NGC 6803. Various forbidden and permitted lines, e.g. HI, HeI, HeII, [OIII], [NII], [ArIII], and [SII], indicate complicated but systematic physical conditions variation: electron temperatures $T_\epsilon \sim 9000 - 11\,000$ K and electron number densities $N_\epsilon \sim 2000 - 9000$ cm^{-3}. The line profile analysis of these ions also indicates the systematic change or the acceleration of the expansion velocities in the range of $10 - 22$ km s^{-1}. We show that the velocity gradient and physical condition found in various ions are closely related to the prolate ellipsoidal structure of NGC 6803. The expansion velocity and the ionic abundance of O^{2+} were derived based on the OII and [OIII] lines. In spite of the discrepancy of ionic abundances derived by the two cases and their line profiles, the expansion velocities of them agree well. We find that the ratios of the red to blue line component of the HeII & OII lines are different from those of the [OIII] or other forbidden lines that indicates a possible involvement of emission of HeII & OII lines. This subtle difference and the different physical condition of the lines are likely to be caused by the elongated geometry and the latitude dependence of the emission zone.

Key words : Planetary Nebula, Interstellar Matter (ISM), Spectroscopic observation, Kinematics, NGC 6803

I. INTRODUCTION

The chemical abundance of the interstellar matter (ISM) provides an important clue in establishing the Galactic chemical evolutionary scenario. Young stars have been newly born from such ISM that consists of materials released by dying stars. In this respect, the understanding of the mechanism of the mass loss of an intermediate star of $1 - 6$ $M_\odot$ at its last stage of evolution, and its shaping into a planetary nebula (PN) would be interesting. The planetary nebula NGC 6803, located near the Galactic plane (l=46°, b =4.1°) at a distance of about 2 kpc, is known as an object receding from us with $V_r = 11.3 - 14.9$ km s^{-1}. The overall shape of the main shell is an elliptical ring, whose size is about $6''\times4''.5$. A PN emits various forbidden lines from UV to IR wavelengths, but in occasion it also shows some permitted lines. NGC 6803 is known to be an object of permitted lines such as OII, NII, similar to the well known Saturn nebular NGC 7009. We derive the expansion velocities of the ions and their physical conditions based on various forbidden and permitted lines secured with the Hamilton Echelle Spectrograph (HES) at Lick observatory.

In §2, the observations of the HES spectral data are summarized. Spectral data analysis and variation of expansion velocities vs. ionic potential energy are given in §3. In §4, we give a brief conclusion for our study.

Corresponding Author: S. Hyung

II. OBSERVATIONS AND DATA ANALYSIS

Our optical data were obtained with the HES at the Coudé focus of the 3m Shane Telescope of the Lick Observatory on 1995 August 18 (UT) and 2001 August 29 (UT), respectively. We obtained long and short exposures, i.e. 120 & 2 minutes in 1995 and 60 & 3 minutes in 2001, respectively. Although we referred to both data, we used the 1995 spectra in this study. The typical seeing was about $\sim1''.0$. We used a large 2048×2048 pixel CCD, which covered the whole HES echelle spectral pattern at a single exposure. The spectroscopic slit employed was 640 μm in width, which amounted to $\sim1''.4$ for image size at the Hamilton Telescope Coudé focus. For this slit width, the limiting resolution on the CCD chip was about 2 pixels, which correspond to $\triangle\lambda$ = 0.05 & 0.15Å at 3600 & 8850Å, respectively. The slit length of $5''$ was chosen to avoid confusion of successive echelle orders.

For spectral calibration, we took exposures of a Th-Ar arc lamp to set the wavelength dispersion scale, exposures of a dome-quartz lamp to fix a flat field that allowed us to correct for pixel-to-pixel sensitivity fluctu-

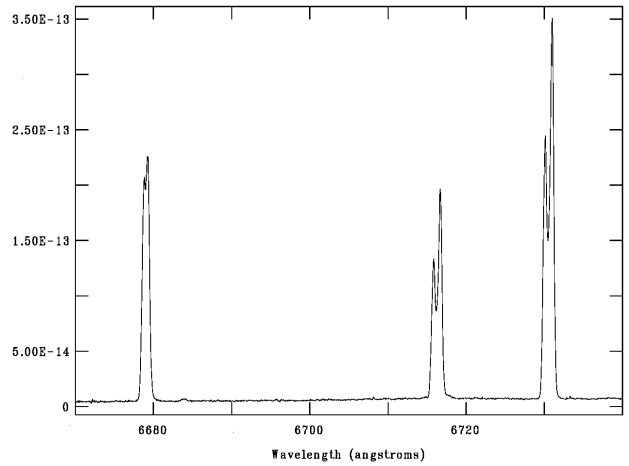

Fig. 1.— The final HES Spectra in the 6670 – 6740Å range, showing 3 prominent HeI6678, [S II]6717,30 lines (Exposure = 120 minutes; 1995 August 18, UT). Note that the red components are stronger.

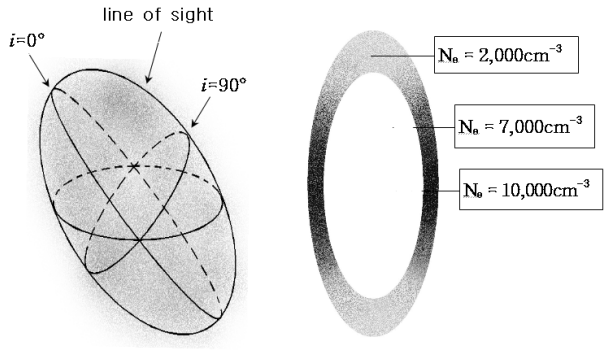

Fig. 2.— Schematic model geometry of NGC 6803. Left: a prolate ellipsoid. Right: an edge-on view cross section.

ations, and finally, exposures on the 2 standard stars of known spectral energy distribution, i.e. BD+28°4211 & 58 Aql. These standard stars were observed with a slightly larger slit size 1.″8×5″ to eliminate atmospheric dispersion effects served as spectrophotometric standards.

With the National Optical Astronomy Observatory IRAF echelle data reduction package, we extracted nebular spectral lines from raw images, employing Th-Ar maps to identify lines. The data reduction procedures are described in Hyung (1994). In Fig. 1, we present one spectral scan to show the quality of our HES data, taken from the 120 minute (or 2 hour) exposure. We chose the 2 hour exposure, since the spectral image with relatively long exposure would give high quality signal to noise ratios even for the permitted lines of weak intensity. We also needed the additional 2 minute short exposure to avoid the saturation for the stronger lines. To fix the interstellar reddening, we corrected the observed fluxes with an extinction coefficient of C=0.63 or $A_v = 1.3$ [$C = \log \mathrm{I(H}\beta)/\mathrm{F}(\beta)$]. This extinction parameter is obtained from a comparison of the observed Balmer line ratios and Balmer vs. Paschen line ratios with the theoretical ones (assuming T_ϵ =10 000 K).

Table 1 gives the electron temperatures and densities of NGC 6803, obtained from the diagnostic line ratios. Detailed descriptions on how to derive the physical condition based on the strategically important diagnostic lines are given in Hyung (1994). Except for that of [NI], the electron densities are 5000 – 9000 cm^{-3}. The electron temperature of the lower excitation [NII] line is higher than that of the high excitation lines, [OIII] or [ArIII]. This could be due to hardening of the UV photons at the outer shell boundary: The soft UV photons are generally absorbed first in the inner shell and as a result, the gases in the outer shell would be ionized by the remaining hard UV photons, resulting a high electron temperature at the edge of the shell. We assume N_ϵ = 8000 cm^{-3} in finding the electron temperatures, T_ϵ, whereas we use T_ϵ = 9700 K for a derivation of electron density, N_ϵ.

In this investigation, we will concentrate the expansion velocities obtained from the line profile analysis. Hence, we do not list the whole number of lines. The detailed analysis for the whole line list will be given in the other abundance study in the near future.

Since NGC 6803 is an ellipsoidal geometry, the different electron temperatures and densities found from the different ions and their ionic stages must be related to a radial distance of the emitting region from the central star of planetary nebula (CSPN) due to the axial distance difference. In the prolate hollow ellipsoid, there are two distinct regions: the equatorial region (closer to the CSPN) and the distant polar region. The density of the former equatorial zone must be higher than that of the latter polar cone. Fig. 2 shows the schematic model geometry of NGC 6803 (the observer is e.g. at $i \sim 50°$) and its cross-section (edge-on view). If we correspond the diagnostically derived physical condition to the model geometry, the lines of high electron density must be coming from the equatorial zone, e.g. with $N_\epsilon \sim$ 10 000 cm^{-3}, while the lines of low density from the polar shell, e.g. with $N_\epsilon \sim$ 2000 cm^{-3}. We do not try to allocate the electron temperatures to the model geometry, though, since there seems to be a temperature reversal zone, i.e. T_ϵ([NII]) > T_ϵ([OIII]) due to the excitation of the hardened UV photons in the outer shell boundary.

III. ANALYSIS OF LINE PROFILES

Fig. 3 displays the line profiles of [OIII]5007, which shows a double peak line profile. The line intensity from the redshift (or receding) component, is stronger than that of the blueshift one. Using the Starlink Dipso, we decomposed the line profiles; and we measured each

Table 1.
Diagnostic line ratios and physical conditions

Ion	Lines	Ratio	T_ϵ, N_ϵ
[O III]	I(λ4959 + λ5007)/I(λ4363)	225.9	9700 K
[N II]	I(λ6548/84)/I(λ5755)	71.2	11 000 K
[Ar III]	I(λ7136 + λ7751)/I(λ5191)	273.3	9000 K
[N I]	I(λ5198)/I(λ5200)	1.54	2000 cm^{-3}
[O II]	I(λ3726)/I(λ3729)	2.31	5000 cm^{-3}
[Cl III]	I(λ5538)/I(λ5518)	1.71	8000 cm^{-3}
[S III]	I(λ6731)/I(λ6716)	1.91	9000 cm^{-3}

N_ϵ: found assuming T_ϵ = 9700 K.
T_ϵ: found assuming N_ϵ = 8000 cm^{-3}.

line center, full width at half maximum (FWHM), and fluxes. The measured values for [OIII]5007, [NII]6583, & [SII]6731 are given in Table 2. The flux ratio of the red to blue components is 1.2 – 1.4. Although NGC 6803 appears to be a fairly symmetrical ellipsoid, the detailed structure is perhaps not simple. These 3 and most other lines imply that the receding shell of NGC 6803 has a stronger emission than the approaching one. From the separation of the two peaks in the decomposed line profiles as in Fig. 3, one can directly estimate the expansion velocity, $V_{exp}(\triangle p)$. Meanwhile, one can also estimate the expansion velocity, V_{exp}, based on the FWHM of the single line profile (① – ①′). Such derivations for 3 lines are also given in the last two columns of Table 2 (detailed method follows).

Since the PN itself consists of many stratified shells of different expansion velocities, the width of the integrated line profiles will become wider. The emission lines also subject to broadenings by various other sources. These sources are (1) natural broadening, V_n; (2) thermal broadening, V_{th}; (3) instrumental broadening, V_{inst}; (4) fine structure broadening, V_{fs}; and (5) turbulence, V_{trb}. Correcting these sources, we can estimate the pure shell expansion velocity, V_{exp} using

$$V_{FWHM} \simeq (2V_{exp})^2 + {V_{th}}^2 + {V_{inst}}^2 + {V_{fs}}^2 + {V_{trb}}^2.$$

To estimate the spectrograph's instrumental broadening, $V_{inst} = c \cdot \frac{\triangle\lambda}{\lambda}$, we measured the unsaturated Th-Ar lamp line FWHM of the Lick HES system, i.e. V_{inst} = 7.892 km s^{-1}. Thermal broadening velocity can be found from $V_{th} = (8kT_e\ \ln 2/m)^{0.5} = 21.6 \times 10^{-2} \times T_e^{0.5} m^{0.5}$ km s^{-1} (Clegg *et al.* 1999), where k is the Boltzman constant and m atomic weight. In estimating the thermal broadening, we assumed the electron temperature T_e = 9700 K (see Table 1). For the Hα fine structure, we refer to Clegg *et al.* (1999). For other permitted lines, we assume V_{fs} = 5 km s^{-1}, while for the forbidden lines, we ignore, i.e. 0 km s^{-1} (see Sabbadin *et al.* 2004, 2005, 2006). For the turbulence, we applied V_{trb} = 5 km s^{-1} only to the forbidden lines (Sabbadin *et al.* 2006).

Table 3 lists the expansion velocities for a whole series of ions. Successive columns are ions, line wavelengths, V_{FWHM}, V_{fs}, V_{trb}, and V_{exp} in km s^{-1}. The last two columns are the two peak wavelength separation, $\triangle$p, and $V_{exp}(\triangle p)$. For the case of HI recombination lines, twelve lines are available, while some ions such as [Cl II], have only one line. Forbidden lines are [N II], [OI], [OII], [OIII], [NeIII], [S II], [S III], [Cl II], [Cl III], [Cl IV], [Ar III], [Ar IV], [K IV], and [Fe II], while the recombination lines are HI, HeI, HeII, CII, NII, NIII, OII, SiII, and MnI. Some ions identified in the present work had been unreported in the earlier studies.

The number of lines used in deriving the velocities are different for each ion. For example, we used 12 Paschen lines for HI, while we used 4 lines, i.e. $\lambda\lambda$7281, 7065, 6678, & 5876, for HeI. Using the derived expansion velocities in Table 3, we obtained the mean values for each ion. In Table 4, we list the mean values of expansion velocities vs. ionization potential (IP) to see the variation of the expansion velocities. Fig. 4 shows the plot of the expansion velocities vs. decreasing IP. The velocity diagram shows that the high excitation ions of high IP are emitted close to the CSPN, while the low excitation ions are emitted farther out from the center. If the PN geometry is a sphere, one can easily assume that the speed of the nebular gas increases with distance from the CSPN (Wilson 1950).

Since the PN NGC 6803 is ellipsoidal, the prolate geometry must play an important role not only for the density contrast structure but also for the expansion velocity gradient in the pole axis. Thus, we consider the additional factor of the radial distance from the CSPN to the shell, in addition to the radially outward acceleration. With the ellipsoidal geometry mentioned in Fig. 2, the distant polar shell is assumed to be a zone responsible for the lower density diagnostic lines, while the closer equatorial shell to be a zone for the high density diagnostic lines. The proposed density contrast structure between the polar conic zone and the equator is well known in many previous studies, e.g. Mellema (1997). The former polar zone is bipolar caps,

Table 2.
Flux and expansion velocity from decomposed double peak line profiles

Ion	λ (Å)	Comp.	λ (Å)	FWHM (Å)	Flux (erg Å^{-1} s^{-1} cm^{-2})	V_{exp} (km s^{-1})	$V_{exp}(\triangle p)$ (km s^{-1})
[OIII]	5006.84	blueshift	5006.809	0.417	2.886(-11)		
		±	0.004	0.005	5.689(-13)		
		redshift	5007.208	0.412	3.298(-11)		
		±	0.003	0.004	5.749(-13)	22.13	11.95
[NII]	6583.45	blueshift	6583.968	0.660	1.852(-12)		
		±	0.005	0.011	2.640(-14)		
		redshift	6584.796	0.557	2.536(-12)		
		±	0.003	0.006	2.540(-14)	33.04	18.86
[SII]	6730.85	blueshift	6730.128	0.639	8.118(-14)		
		±	0.004	0.010	1.005(-15)		
		redshift	6730.971	0.551	1.053(-13)		
		±	0.003	0.006	9.516(-16)	28.76	18.77

$X(-Y)$ in column (6) implies $X \times 10^{-Y}$.

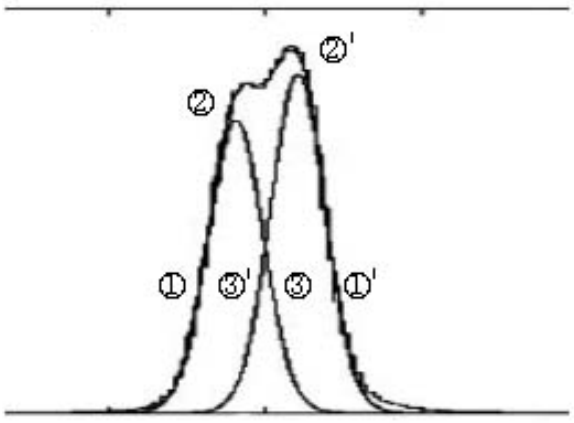

Fig. 3.— Decomposition of the [OIII]5007 line profile. See Fig. 5 for the emitting zones, corresponding to the 6 positions of the line profile. The wavelength differences between two peaks, △p, can be measured from the de-convolved profile. (△p =② −②′)

while the latter equatorial zone can be represented as a torus ring. The radially outward accelerated expansion still works in this new interpretation. However, the expansion is expected to be faster in the polar direction. In Fig 5, we arrange the ions in the cross-section of the proposed prolate geometry: the emission loci of various low to high ions are marked in this cross-section diagram. The velocity gradient, V_{exp} vs. IP, and the higher electron or gas density with latitude can now be simultaneously accommodated together in this cross-section diagram. More detailed study would be desirable with some high spatial resolution images taken with the more sophisticated telescope, e.g. Hubble Space Telescope camera, though.

Table 4.
Expansion velocities vs. IP

Ion	IP (eV)	V_{exp} (km s^{-1})	$V_{exp}(\triangle p)$ (km s^{-1})
[OI]	0	30.92	21.70
[S II]	10.4	28.76	18.77
[OII]	13.6	19.02	17.43
HI	13.6	20.07	11.42
[N II]	14.5	30.34	18.55
[S III]	23.3	24.64	14.06
CII	24.4	19.17	10.64
HeI	24.6	21.60	12.01
[Ar III]	27.6	23.67	13.17
NII	29.6	21.50	11.59
OII	35.1	23.22	11.65
[OIII]	35.1	22.13	11.95
[Ar IV]	40.7	17.80	10.69
[NeIII]	40.9	21.98	12.43
NIII	47.4	15.73	*
HeII	54.4	19.27	10.16

IP: ionization potential.

NGC 6803 is about $6'' \times 4\farcs5$ in angular size, so the equatorial angular radius would be $2\farcs25$. If the distance is known, the polar radius can be easily inferred. The polar radius however, cannot be calculated from the observed angular radius of $3''$ unless the inclination angle (i) is known. As in Fig. 2 & Fig. 5, if we introduce an inclination of $i = 50°$ of the axis relative to the line of sight, the r_a/r_b of the PN would be about 1.8. One cannot evaluate the exact inclination of any individual object, but the average value for randomly

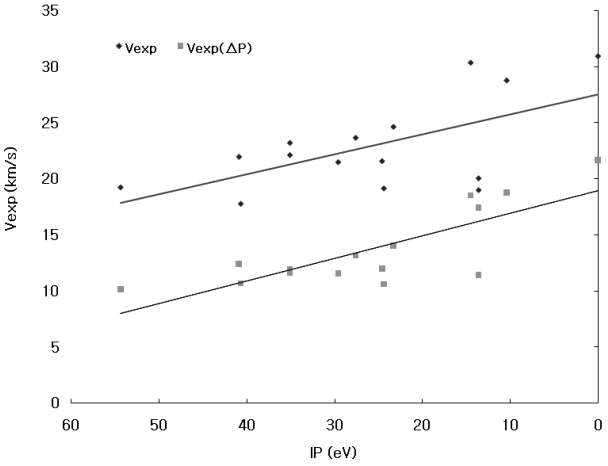

Fig. 4.— Expansion velocity vs. ionization potential. The velocities of lower excitation lines are faster than those of the high excitation lines.

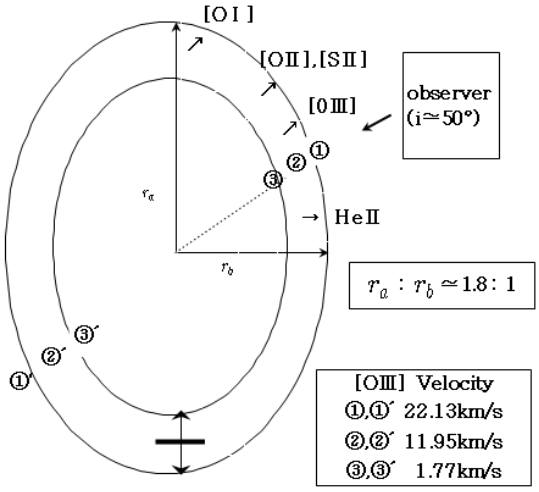

Fig. 5.— A schematic model geometry. See the [OIII] line profile in Fig. 3.

distributed bilaterally symmetric objects can be statistically derived as $i \simeq 57°$. Our assumed inclination (or r_a/r_b) is slightly smaller than this statistical mean value. This choice would not change our conclusion, though.

For an assumed distance of 2 kpc, the polar and equatorial shell radii would then be 0.034 & 0.019 pcs. By looking at the optical appearance of the PN, the rim or shell thicknesses are assumed to be 0.009 & 0.005 pcs (about 1/3 – 1/4 of the outer shell radii). The [OI], [OII], & [SII] are strongest near the polar cap, while the HeII and other high excitation lines are stronger near the equator. However, the inner shell boundary of the polar cap might be a small amount of high to medium excitation lines. One expects that the medium excitation lines such as [OIII]5007 are dominant in the middle latitude zone, though!

Many PNe showed an evidence of faster expansion speed in the polar direction, especially prominent in the case of bi-polar or butterfly shaped objects like NGC 2440 (Hyung & Aller 1998). Most lines have two components, the blue and the red. If the polar cap is responsible for the [OI] emission and if the observer is looking at the PN from the polar axis ($i = 0°$), the blueshift portion is expected from the expanding shell close to the observer, while the redshift portion is from the other outwardly expanding (located on the farther side of the outwardly expanding shell). We further divide each cap into 3 sub zones: the (slowly expanding) inner boundary (r $\sim$ 0.025 pc); middle zone (r $\sim$ 0.030 pc) with medium or average speed shell, and the swiftly expanding outer edge shell (r $\sim$ 0.034 pc). The same can be applied to the high excitation HeII emitting equatorial shell: e.g. 9.95 km s^{-1} at the inner shell of 0.014 pc, $\sim$15 km s^{-1} at 0.0165pc; and 17.51 km s^{-1} at the outer shell of 0.019 pc. For the medium excitation line [OIII], the differences are larger, 1.77, 11.95, & 22.13 km s^{-1}. Such velocity differences are expected, since the shell of gas would be accelerated right after leaving the surface of the CSPN a few thousand years before it reaches the terminal velocity (see Hyung, Aller, & Feibelman 1993; Castor, Lutz, & Seaton 1981).

The exact expansion velocities cannot be obtained from the observed radial velocities, since we do not know the true inclination angle of the object. If the assumed geometry with $i = 50°$ is truly the case for NGC 6803, we may be able to roughly estimate the correction factor from the model geometry: the expansion velocities of low excitation lines (emitted from the polar caps) can be increased up to 56% or by about 1/cos$i$ or 1.56, while those of high excitation lines (emitted from the equatorial zone) up to 30% or by about 1/sin$i$ or 1.3. However, this figure or factors are highly speculative, since we do not know the exact projection angle of the ellipsoidal shell. Nonetheless, the actual expansion velocities are obviously higher than the values given in Tables 3 & 4.

IV. COLLISIONAL AND RECOMBINATION LINES FROM THE SAME IONS?

Since the launch of IUE satellite, it has been a long standing problem that the chemical abundance derived from the recombination lines is not in agreement with that of the forbidden lines. Although the chemical abundance derivation for all the available lines is beyond the current limit, we will check ionic abundances of O^{2+} derived by different lines. The O^{2+} ionic abundance for recombination lines can be derived from

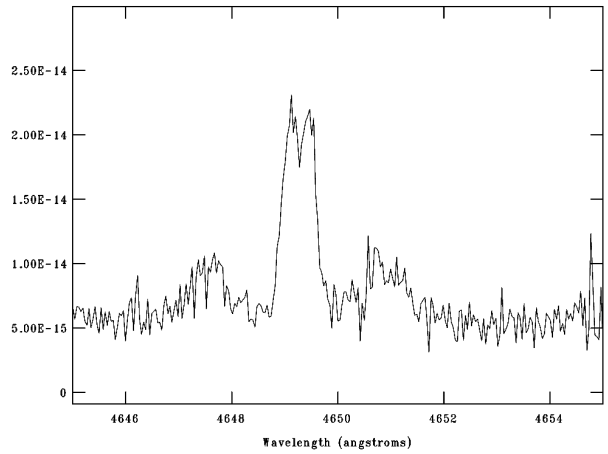

Fig. 6.— The line profile of OII4649. Compared to the [OIII]5007 in Fig. 3, the blue component is stronger than the red one.

$$O^{2+}/H^{+} = \frac{\lambda}{4861}\frac{\alpha(H\beta)}{\alpha(\lambda)}\frac{I(\lambda)}{I(H\beta)}, \qquad (1)$$

where $\alpha(\lambda) = \alpha_j B(\lambda)$. Here, the branching ratio B(λ) is adopted from Liu *et al.* (1995); and the recombination coefficients $\alpha(H\beta)$ & α_j are calculated using the Péquignot *et al.* (1991) and Storey (1994) formulae, respectively, assuming the physical condition of T_ϵ=9680 K & N_ϵ = 7940 cm^{-3}. We found O^{2+}/H^{+} = 1.98×10^{-3} [I(OII4072)=0.477]. This value roughly agrees with the derivation by Wesson *et al.* (2005), 1.439×10^{-3}. From the [OIII] collisional excitation lines with the atomic data given in Hyung & Feibelman (2004), we also found O^{2+}/H^{+} = 4.23×10^{-4} from [OIII] lines: i.e. I(4363)=6.42; I(4959)=355.97; and I(5007)=1095.28. As found in other PNe, the ionic abundance derived from the recombination line is about 5 times larger than that from the forbidden lines.

Fig. 6 shows the spectrum of OII4649 which clearly displays the double peaks. From the OII4649 profile, we were able to measure both velocities which can be compared with that of the [OIII] lines (see Table 3). There are two other weak OII lines, λ4651 & λ4072, available for our study. The former is too weak to trace the line profile, while the latter is fairly good to measure its FWHM (but not measurable the double peaks). From the latter, we also derived the expansion velocity based on the FWHM. Note that expansion velocities derived from OII4649,4072 and [OIII]4959,5007 are quite similar, i.e. $V_{exp} \sim 22.7$ km s^{-1}.

The line profile shapes of both OII4649 and [OIII]5007 imply that the emissions might be coming from the same shell. Are the forbidden & permitted lines emitted from the zone of the same physical condition? We inspect the intensity ratio of the redshift to blueshift component: the OII4649 component gives ~0.78, while the [OIII]5007 gives about 1.14. Note that the blueshift line profile or the approaching component in the permitted OII line intensified for some unknown reason.

The reversed red to blue component ratio or the stronger blueshift component of the OII line is hard to understand, considering that most other collisional lines show the same trend. So, there are two possibilites with the OII emission: (1) it could be from the same shell of the [OIII] lines; (2) it could different shells of different latitudes or different orientation, although their distances and the expansion velocities are about the same. The latter case of the geometrical effect might affect the emission strength. If the orientation or the latitude of the emitted zone of the OII lines is different from that of [OIII] lines, one cannot assume that their physical condition, i.e. electron temperature and density, is the same in calculating the ionic abundance estimation. The O^{2+}/H^{+} ionic abundance derived from the permitted lines is about 5 times larger than that derived from the forbidden lines. The answer to this discrepancy may be found from the line profile shape, i.e. stronger blue component of OII lines. Note that the expansion velocities of high excitation HeI or HeII lines are similar to those of OII or [OIII] lines (see Table 3). Table 5 lists the blue to red component line ratios of HeI, HeII, and OII. The HeI value in Table 5 is similar to the other forbidden lines (see Table 2), but the HeII value appears to be similar to the OII one. The blue or approaching component is stronger than the red one in HeII & OII. The zone responsible for HeII emission is perhaps the same as that of the OII emission.

Barlow *et al.* (2006) found the expansion velocities of the OII lines were smaller than those of the [OIII] lines in two PNe, NGC 7009 and NGC 6153. If so, the OII lines are emitted from the inner shell. They concluded that [OIII] and OII lines cannot originate from the same identical zone. Although the expansion velocities seem to indicate that both might have been formed in the same zone, the line profiles suggest that they are from different zone of different orientation or different latitude. The present 2 hour exposure did not give good S/N profiles especially in the case of weakly registered permitted lines. These weakly measured permitted (or recombination) lines should be analyzed further in future studies when they are available in a much longer exposed spectral image.

Several scenarios have been proposed to solve this discrepancy in some PNe: temperature fluctuations (Peimbert 1967), existence of high density component (Zhang *et al.* 2005), and existence of hydrogen-deficient cold component (Jacoby & Ford 1983). The other possible line emission mechanisms are a fluorescence by the stellar UV photons or an ionic abundance enhancement due to the charge exchange with H ions. To verify the validity of these scenarios, we compared the expansion velocities derived by the collisional and recombination lines, hoping to clarify the issue. The expansion velocity indicates that they are likely to be from the same zone, while the line profile implies that they are from

TABLE 5.
FLUXES OF HEI, HEII, AND OII

Ion	λ (Å)	Comp.	λ (Å)	FWHM (Å)	Flux (erg Å^{-1} s^{-1} cm^{-2})	r/b
HeI	6678.15	blueshift	6678.75	0.535	1.038(-13)	
		±	0.01	0.006	1.618(-15)	
		redshift	6679.27	0.510	1.117(-13)	
		±	0.01	0.005	1.620(-15)	1.076
HeII	4685.68	blueshift	4686.46	0.384	4.844(-14)	
		±	0.01	0.001	1.181(-14)	
		redshift	4686.77	0.275	3.167(-14)	
		±	0.01	0.001	1.181(-14)	0.654
OII	4649.14	blueshift	4649.110	0.355	5.668(-15)	
		±	0.025	0.041	7.230(-16)	
		redshift	4649.471	0.285	4.423(-15)	0.780
		±	0.018	0.036	7.186(-16)	

$X(-Y)$ in column (6) implies $X \times 10^{-Y}$.
See Tables 3 & 4 where the expansion velocities derived for these 3 ions are similar.

different zone or shell of different orientation.

V. CONCLUSION

We have investigated expansion velocities, physical conditions, and structure of NGC 6803, based on the collisional and permitted lines. The stratification effect and the acceleration of the gas are well known in many PNe (Aller 1956; Wilson 1950). Our expansion velocity vs. IP diagram also shows a presence of acceleration in NGC 6803. To explain the variation of expansion velocities and physical condition in a self-consistent way, we proposed a co-relationship between physical condition of the ions and their latitude or location in the axisymmetric prolate geometry.

We found the same expansion velocity from the [OIII] & OII lines, based on their FWHM and Doppler peaks, respectively. This result is different from those of the other PNe such as NGC 7009 & NGC 6153. The careful inspection of the intensity ratio of the redshift to blueshift lines implies that the above O^{2+} lines are originated from different zone in an ellipsoidal geometry, though. The ellipsoidal geometry is likely to play an important role in line formation, as in the case of symbiotic star or a certain PN, e.g. Lee & Hyung (2000). We conclude that the permitted lines of OII have been formed in a much restricted zone near the equatorial torus shell (i.e. HeII zone), while the [OIII] lines have been emitted from a broader area of the middle latitude of the shell. Ionic abundance discrepancy problem between the permitted lines and the collisional lines must be reexamined more carefully in future studies.

Since a large fraction of PNe show bi-lateral symmetries, the proposed expansion velocity and physical condition difference found from various lines and their latitudinal relation could be applicable to other similar planetary nebulae, as well. In case of bipolar PNe or other irregular PNe which might have been evolved from massive progenitors, the situation would be more complicated. Not only the expansion velocities but also the comparison of the red to blue line components would provide a clue for PN structure and chemical abundance discrepancy problem. This, however, must await the availability of much sophisticated observational spectra of high S/N ratio.

ACKNOWLEDGEMENTS

This work was supported by the research grant of Chungbuk National University in 2008. S.H. is grateful to the late Prof. Lawrence H. Aller of UCLA, who carried out the Hamilton Echelle observation program together. The authors also acknowledge the anonymous referee for his/her careful review of this paper; and Eugenia H. of Ohio State University for her careful reading.

REFERENCES

Aller, L. H., 1956, Gaseous Nebulae (London: Chapman & Hall)

Barlow, M. J., Hales, A. S., Storey, P. J., Liu, X.-W., Tsamis, Y. G., & Aderin, M. E., 2006, bHROS high spectral resolution observations of PN forbidden and recombination line profiles, IAU Symposium, 234, 367

Castor, J. I., Lutz, J. H., & Seaton, M. J., 1981, Ultraviolet spectra of planetary nebulae. III - Mass loss from the central star of NGC 6543, MNRAS, 194, 547

Clegg, R. E. S., Miller, S., Storey, P. J., & Kisielius, R., 1999, Recombination Line Intensities for Hydrogenic Ions: The fine-structure components of HI and HeII, A&A, 135, 359

Hyung, S., 1994, Density contrast shell models for the planetary nebula IC 2165, ApJS, 90, 119

Hyung, S. & Aller, L. H., 1998, The Optical Spectrum of the Planetary Nebula NGC 2440, PASP, 110, 466

Hyung, S., Aller, L. H., & Feibelman, W. A., 1993, The spectrum of the planetary nebula NGC 6567, PASP, 105, 1279

Hyung, S. & Feibelman, W. A., 2004, Optical and IUE Spectra of the Planetary Nebula NGC 7026, ApJ, 614, 745

Jacoby, G. H. & Ford, H. C., 1983, The hydrogen-depleted planetary nebulae Abell 30 and Abell 78, ApJ, 266, 298

Lee, H. W. & Hyung S., 2000, Broad Hα Wing Formation in the Planetary Nebula IC 4997, ApJ, 530, 49

Liu, X. W., Storey, P. J., Barlow, M. J., & Clegg, R. E. S., 1995, The rich OII recombination spectrum of the planetary nebula NGC 7009: new observations and atomic data, MNRAS, 272, 369-388

Mellema, G., 1997, The formation of bipolar planetary nebulae, A&A, 321, 29

Peimbert, M., 1967, Temperature Determinations of H II Regions, ApJ, 150, 825

Péquignot, D., Petitjean, P., & Boisson, C., 1991, Total and effective radiative recombination coefficients, A&A, 251, 680-688.

Sabbadin, F., Turatti, M., Cappellaro, E., Benetti, S., & Ragazzoni, R., 2004, The 3-D ionization structure and evolution of NGC 7009 (Saturn Nebula), A&A, 416, 955

Sabbadin, F., Benetti, S., Cappellaro, E., Ragazzoni, R., & Turatto, M., 2005, The 3-D shaping of NGC 6741: A massive, fast-evolving Planetary Nebula at the recombination-reionization edge, A&A, 436, 549

Sabbadin, F., Turatto, M., Ragazzoni, R., Cappellaro, E., & Benetti, S., 2006, The structure of planetary nebulae: theory vs. practice, A&A, 451, 937

Storey, P. J., 1994, Recombination coefficients for OII lines at nebular temperatures and densities, A&A, 282, 999-1013

Wesson, R., Liu, X. W., & Barlow, M. J., 2005, The abundance discrepancy - recombination line versus forbidden line abundances for a northern sample of galactic planetary nebulae, MNRAS, 362, 424-454

Wilson, O. C., 1950, A Survey of Internal Motions in the Planetary Nebulae, ApJ, 111, 279

Zhang, Y., Liu, X.-W., Luo, S.-G., Péquignot, D., & Barlow, M. J., 2005, Integrated spectrum of the planetary nebula NGC 7027, A&A, 442, 249

TABLE 3.
EXPANSION VELOCITY

Ion	λ(Å)	V_{FWHM}	V_{fs}	V_{trb}	V_{exp}	$\triangle$p	$V_{exp}(\triangle p)$
HI	10049.4	50.76	7.591		22.39	0.837	12.50
	9545.97	40.54	7.618		16.36	0.641	10.08
	9014.91	47.25	7.591		20.38	0.620	10.32
	4861.33	43.81	7.618		18.35	0.384	11.85
	6562.82	45.25	7.618		19.20	0.465	10.63
	8862.79	48.40	7.591		21.04	0.675	11.42
	8750.48	44.91	7.618		19.00	0.685	11.74
	8598.39	46.75	7.591		20.08	0.672	11.72
	8665.02	47.78	7.591		20.68	0.653	11.31
	8468.26	49.24	5.591		21.52	0.647	11.46
	8502.49	49.05	5.591		21.41	0.667	11.77
	8545.38	47.40	5.591		20.46	0.700	12.29
					20.07±1.64		11.42±0.74
HeI	7281.35	49.02	5		23.47	0.559	11.51
	7065.28	42.89	5		20.24	0.591	12.55
	6678.15	44.47	5		21.08	0.520	11.68
	5875.67	45.44	5		21.59	0.482	12.30
					21.595±1.37		12.01±0.49
HeII	4685.68	37.77	5		17.51	0.311	9.95
	5411.52	44.35	5		21.02	0.374	10.37
					19.265±2.48		10.16±0.30
CII	4267.18	37.26	5		17.77	*	*
	6578.03	41.95	5		19.75	0.483	11.01
	7231.12	41.49	5		19.98	0.495	10.27
	7236.19	39.38	5		18.88	1.312	27.19
					19.17±1.21		10.64±0.52
[N II]	6548.03	56.35		5	27.64	0.796	18.23
	6583.45	66.97		5	33.04	0.828	18.86
					30.34±3.82		18.545±0.44
NII	5679.59	44.37	5		21.50	0.439	11.59
NIII	4379.11	32.13	5		15.11	*	*
	4097.31	34.48	5		16.35	*	*
					15.73±0.88		
[OI]	6300.3	61.90		5	30.48	0.922	21.95
	6363.78	63.64		5	31.36	0.910	21.45
					30.92±0.62		21.7±0.35
[OII]	3726.03	39.53		5	19.02	0.433	17.43
OII	4072.16	53.41	5		26.16	*	*
	4649.14	41.94	5		20.27	0.361	11.65
					23.215±4.16		
[OIII]	5006.84	45.54		5	22.13	0.399	11.95
	4958.92	47.18		5	22.97	0.431	13.03
					22.55±0.59		12.49±0.76
[NeIII]	3868.71	46.52		5	22.66	0.326	12.64
	3967.41	43.85		5	21.29	0.323	12.21
					21.975±0.97		12.425±0.30
SiII	6347.09	45.85	5		22.35	0.512	12.10
	6371.36	40.49	5		19.60	0.484	11.39
	5041.06	38.56	5		18.60	*	*
					20.18±1.94		11.745±0.50
[S II]	6730.85	58.39		5	28.76	0.842	18.77
[S III]	9068.9	28.38		5	14.19	1.098	18.16
	9531	48.79		5	23.87	0.860	13.54
	6312.1	51.80		5	25.41	0.614	14.59
	6716.47	56.73		5	27.91	0.820	18.31
					24.64±1.09		14.065±0.74

Table 3. Continuued

Ion	λ(Å)	V_{FWHM}	V_{fs}	V_{trb}	V_{exp}	$\triangle$p	$V_{exp}(\triangle p)$
[Cl II]	8578.7	61.55		5	30.37	1.024	17.90
[Cl III]	5517.71	51.10		5	25.06	0.499	13.56
	5537.88	47.67		5	23.30	0.471	12.76
					26.24±3.68		14.74±2.77
[Cl IV]	8046.27	38.03		5	18.34	0.564	10.52
	7530.83	39.44		5	19.07	0.542	10.80
					18.705±0.52		10.66±0.20
[Ar III]	7135.78	48.35		5	23.66	0.615	12.93
	7751.43	48.38		5	23.67	0.693	13.41
					23.665±0.01		13.17±0.34
[Ar IV]	7170.62	35.14		5	16.85	0.514	10.75
	4711.34	38.20		5	18.44	0.304	9.68
	4740.2	38.60		5	18.65	0.353	11.17
	7262.96	35.93		5	17.27	0.540	11.15
					17.80±0.88		10.69±0.70
[K IV]	6101.8	39.82		5	19.28	0.435	10.69
MnI	8926.06	40.93	5		19.87	*	*
[Fe II]	8616.96	20.75		5	9.15	*	*

V_{FWHM}, V_{fs}, V_{trb}, & V_{exp}: in km s^{-1}. V_{th}(km s^{-1}) = 21.26 (H), 10.63 (He), 6.14 (C), 5.68 (5.68), 5.31 (O), 4.75 (Ne), 4.02 (Si), 3.76 (S), 3.58 (Cl), 3.36 (Ar), 3.40 (K), 2.87 (Mn), & 2.84 (Fe). V_{inst} = 7.89 km s^{-1}.